Engineering Fracture Mechanics 168 (2016) 40–57

Contents lists available at ScienceDirect

Engineering Fracture Mechanics

journal homepage: www.elsevier.com/locate/engfracmech

A global/local approach for the prediction of the electric response of cracked solar cells in photovoltaic modules under the action of mechanical loads

M. Paggi [a,*], M. Corrado [b,1], I. Berardone [b]

[a] IMT Institute for Advanced Studies Lucca, Piazza San Francesco 19, 55100 Lucca, Italy
[b] Department of Structural, Geotechnical and Building Engineering, Politecnico di Torino, C.so Duca degli Abruzzi 24, 10129 Torino, Italy

ARTICLE INFO

Article history:
Received 26 February 2015
Received in revised form 12 January 2016
Accepted 13 January 2016
Available online 1 February 2016

Keywords:
Nonlinear finite element method
Laminate
Cohesive zone model
Global/local modeling
Multi-physics
Generalized electric model

ABSTRACT

A numerical approach based on the finite element method to assess the impact of cracks in Silicon solar cells on the electric response of photovoltaic modules is proposed. A global coarse-scale finite element model of the composite laminate is used for carrying out the structural analysis. The computed displacements at the edges of each solar cell are passed via a projection scheme as boundary conditions to a 3D local fine-scale finite element model of the cells which accounts for cohesive cracks. The evaluated crack opening displacements along the crack faces are finally used as input to an electric model characterizing the grid line/solar cell ensemble. The identification of the relation between the localized electric resistance due to cracks and the crack opening, to be used as a constitutive model of cracks, is finally discussed in reference to experimental tests performed in the laboratory.

1. Introduction

The durability of photovoltaic (PV) modules is a relevant issue debated by the scientific community during the recent years [1–3]. It is also subject of intensive discussion by international organizations [4] aiming at providing a rationale for the interpretation of laboratory and field degradation data of PV modules coming from different producers and installed in different climate zones.

After a period of feed-in tariffs promoted by many EU Governments to accelerate investments in the PV sector, PV parks characterized by sufficient energy production in the previous framework are not always adequate to produce profits for the investors within the new regulations. Therefore, it becomes of paramount importance to understand the possible sources of losses in the energy production, quantify the degradation of a PV system, define more accurate business plans accounting for maintenance costs, and eventually invoke warranties when the under performance of PV modules exceeds producers' specifics. Apart from PV parks where installed PV modules have an almost standard layer composition (Fig. 1(a)), the problem of durability is expected to be even more relevant in the next few years due to the rapid progress of building-integrated PV systems. In this case, in addition to energy production, modules have also to guarantee a safe structural performance and

* Corresponding author. Tel.: +39 0583 4326 604; fax: +39 0583 4326 565.
E-mail addresses: marco.paggi@imtlucca.it (M. Paggi), mauro.corrado@polito.it (M. Corrado), irene.berardone@polito.it (I. Berardone).
[1] Present address: Civil Engineering Institute, Materials Science and Engineering Institute, École Polytechnique Fédérale de Lausanne (EPFL), Station 18, CH-1015 Lausanne, Switzerland.

http://dx.doi.org/10.1016/j.engfracmech.2016.01.018
0013-7944/

Nomenclature

$\mathbf{X}$	position vector
$\mathbf{u}$	displacement vector
$\mathbf{d}$	nodal displacement vector
$\mathbf{N}$	shape functions matrix
$\mathbf{R}$	rotation matrix
$\mathbf{g}_{\text{loc}}$	gap vector in the local reference system
g_{n}	crack opening
g_{t}	crack sliding
g_{nc}	critical crack opening displacement
g_{tc}	critical crack sliding displacement
E	Young modulus
ν	Poisson ratio
$\sigma_{\max}$	peak normal cohesive traction
$\tau_{\max}$	peak tangential cohesive traction
l_0	relative displacements at the peak cohesive tractions
r	root mean square of the heights of the crack rough profile
$\mathbf{T}$	cohesive traction vector
$\mathbf{C}$	tangent constitutive matrix
$\mathbf{f}_{\text{crack}}$	residual vector
$\mathbf{K}$	tangent stiffness matrix
V	voltage (V)
I_{tt}	surface current density through the thickness of the solar cell (A/cm^2)
I_{f}	linear current density along the finger (A/cm)
ρ_S	distributed sheet resistance (Ω)
R_{cr}	localized crack resistance (Ω cm)
ξ	local coordinate along the finger
ξ_{cr}	position of the crack along the finger
ξ_0	position of the minimum of the voltage along the finger
V_0	value of the minimum of the voltage along the finger
l	distance between two busbars

other architectonic specifics like shadowing and ambient comfort. These requests lead to customized PV modules with a layer composition tailored to specific needs, see for instance the semi-transparent PV modules used for facades or roofs, Fig. 1(b), or semi-flexible PV modules that can be bonded to curved substrates, Fig. 1(c). For all of these cases, the resistance of Silicon to cracking and durability are important concerns to be scrutinized.

PV modules are laminates composed of thin layers, as schematically shown in Fig. 2. From the lower side towards the upper side exposed to sun we usually have a backsheet (0.1 mm thick) or glass (3 mm thick), a layer of an encapsulant material (typically Epoxy-Vinil-Acetate, EVA, 0.5 mm thick), solar cells (0.16 mm thick) separated in their plane by few millimeters of encapsulant, another layer of EVA like the previous one, and finally a glass cover (3 mm thick) for rigid PV modules, or a polymeric layer like PET (0.2 mm thick) in case of semi-flexible modules.

Commercial modules might have different size and number of cells. In case of modules installed in PV parks, it is common to have a layer with 10×6 square solar cells of about 150 mm side. Solar cells transform the solar radiation in electric energy via the so-called photovoltaic effect [5]. Solar cells are made of monocrystalline or polycrystalline Silicon, a semiconductor able to provide a reasonable energy conversion efficiency of about 15–20% at a relatively low production cost. In the commonly used technology, electrons are collected on the front side of the solar cell by tiny electric conductors called *grid lines* or *fingers* deposited on the cell surface. Two or three *busbars* are soldered on the cell surface and collect the fingers along the direction orthogonal to them, see Fig. 3. These main conductors electrically connect all the solar cells in series. In another technology, to avoid partial shadowing induced by fingers and busbars in order to increase the energy conversion efficiency, a back contact is used and no fingers and busbars are present on the front side. In the present study we restrict our modeling to solar cells with front contacts.

Cracks can originate during various stages from production to installation. They are often invisible with the naked eye but can be accurately identified by the electroluminescence (EL) technique, whose methodology is described in Section 4 where experimental tests are presented. For illustrative purposes, EL images taken by the present authors during various experimental campaigns are shown in Fig. 4. Regardless of the PV technology, cracks can isolate large portions of solar cells by completely interrupting fingers in a worst case scenario, or can just increase the electric resistance related to the finger-solar cell contact at the point where the crack crosses the grid line. Such electrically damaged regions contribute to the drop in the current–voltage curve of the whole PV module and to its electric power-loss.

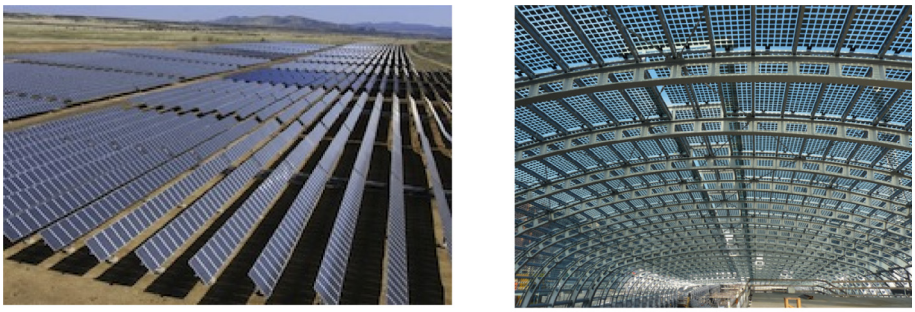

(a) PV park (b) Building-integrated PV

(c) Semi-flexible modules in building-integrated PV

Fig. 1. Photovoltaic parks and new solutions for building-integrated photovoltaics.

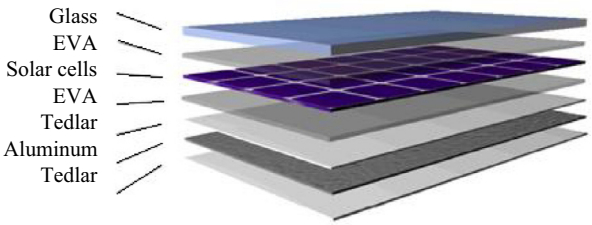

(a)

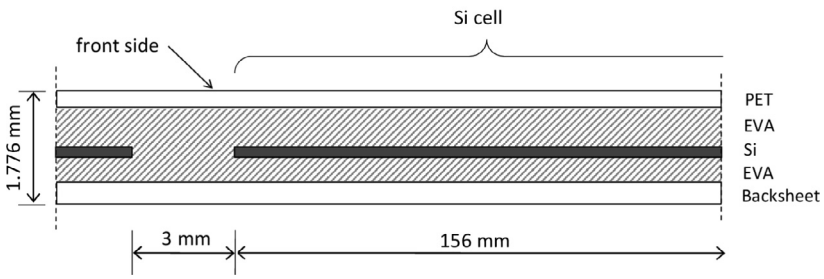

(b)

Fig. 2. (a) A sketch of a PV module with glass cover, and of (b) a semi-flexible PV module with PET cover.

At present we are still far from having a simulation tool able to quantify the impact of cracks on the electric efficiency and durability of PV modules. Under the assumption of a worst case scenario, cracks have been treated in [1] as defects interrupting fingers and leading to insulated portions of the Silicon cell. Using an electric model accounting for the active cell area, an estimate of the maximum possible power-losses has also been made in [1]. In that model, the position and the orientation of cracks with respect to the busbars were found to be key parameters, since they impact on the electric performance in different ways in relation to the size of the portion of the solar cell becoming insulated. Alternatively to the direct experimental approach, a method to estimate the probability of cracking has been proposed in [6] based on the Weibull statistics of Silicon

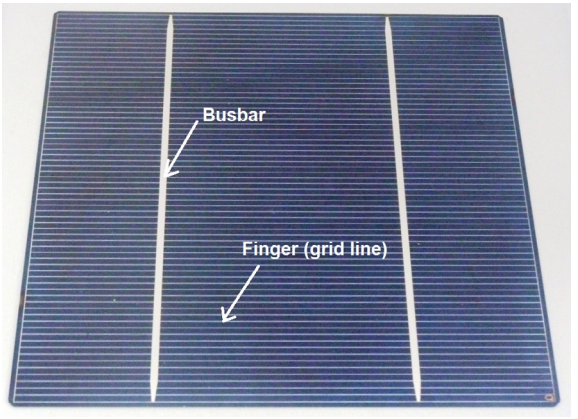

Fig. 3. A photo of a solar cell showing fingers and busbars.

strength and predicting the stress level in solar cells by a linear elastic stress analysis. From the computational point of view, since cracks have a different impact on the electric response depending on the type of solar cell technology (monocrystalline or polycrystalline Silicon), their position with respect to the busbars, and also on the stress state induced by loading, a pioneering multi-physics and a multi-scale finite element approach based on nonlinear fracture mechanics was proposed in [7]. It has also been further extended in [8] by proposing a thermoelastic cohesive zone model to simulate thermomechanical problems in solar cells during cooling after lamination, considering partial heat conduction across crack faces, depending on their opening.

In the present study we propose an advancement with respect to [7] in terms of computational modeling. First, we propose a completely general global/local framework which can be used to handle large size PV modules and provides a more accurate prediction of crack opening. Second, the over-conservative one-diode electric model proposed in [7] with parameters dependent on the potentially electrically inactive area identified by assuming that all the cracks are perfectly insulated lines is herein refined. Namely, we propose an accurate electric model for each finger with localized resistances dependent on the crack opening. We are therefore able to simulate cracks with a degree of electric insulation variable with the load level. Model parameters identification is discussed in Section 4, showing the capabilities of the model to accurately predict the electric response of cracked solar cells embedded in PV modules under the action of mechanical loads. It also elucidates the fundamental mechanisms responsible for the coupling between the mechanical and the electric fields due to cracks. Model parameters identification is finally discussed and the proposal of a perspective coupled electro-mechanical constitutive law for cracks concludes the study.

2. The proposed global/local approach

The global/local approach is a computational strategy often adopted in fiber-reinforced or laminated composites to deal with problems having two very different length scales [9,10], such as the scale of the component and the scale of its microstructure. In general, a homogeneous global or *coarse-scale* model is used to compute the displacement field. The displacements from the global model are taken as boundary conditions for the local model, which is a *fine-scale* representation of a portion of the composite where the material microstructure and its mechanical degradation is simulated with a greater accuracy. In some cases, a feedback from the local model to the global one is required, viz. by updating the global stiffness matrix.

In the present problem, to investigate the effect of realistic loading conditions, it is necessary to simulate the whole composite laminate and the phenomenon of cracking at the cell level, which requires much more details than the global stress analysis. A single fine resolution finite element model able to accurately simulate cohesive cracks in solar cells embedded in the PV module would be computationally too expensive to solve. Moreover, the experimental evidence in [6] shows that cracks have a low impact on the stiffness of the module. Therefore, uncoupling of the global finite element model of the PV module from a local finite element model of each solar cell appears to be a viable choice to reduce the computation cost, allowing also the use of parallel computing schemes for each cell.

On this line of research, in the pioneering attempt in [7], the global model of the PV module to perform linear elastic structural analyses was composed of plate finite elements based on the Kirchhoff theory. The composite structure of the laminate was accounted for by introducing effective elastic properties depending on the stack composition. A 2D local model of each solar cell was then proposed by using plane stress continuum triangular and quadrilateral linear finite elements separated by interface elements along the grain boundaries of polycrystalline Silicon. The global structural analysis provided the out-of-plane displacement w_z and the rotations ϕ_x and ϕ_y in the finite element nodes of the composite plate. These generalized displacements were used to determine the in-plane displacements at the level of each solar cell, to be imposed as boundary conditions to the local model solved under the assumption of plane stress.

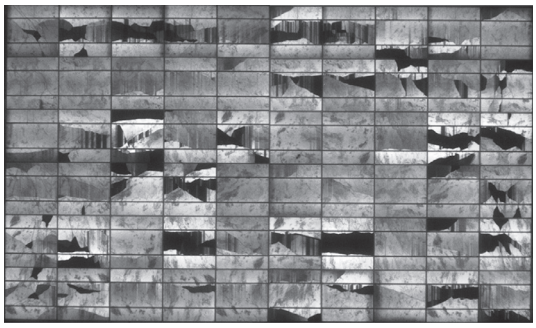

(a) Polycrystalline Si cells

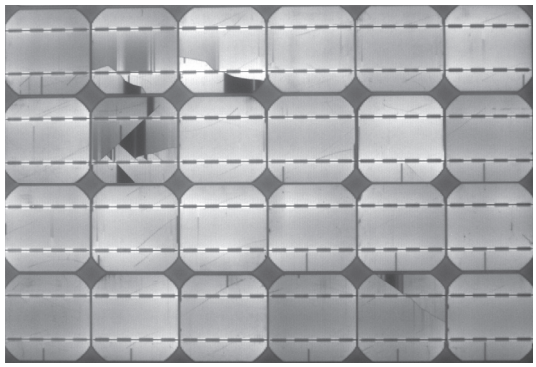

(b) Monocrystalline Si cells

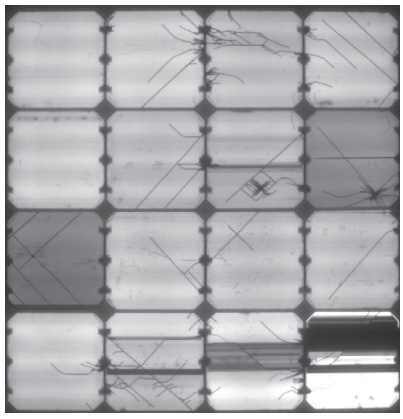

(c) Monocrystalline Si cells with back contacts

Fig. 4. Electroluminescence images showing crack patterns in different PV module technologies: (a) polycrystalline Silicon; (b) monocrystalline Silicon; (c) monocrystalline Silicon with back contacts.

Here, a refined three-dimensional global/local approach is proposed, providing a more accurate description of the physical phenomenon of electric degradation due to cracking, and a more consistent coupling between the coarse-scale and fine-scale finite element models in terms of kinematics.

2.1. The coarse-scale finite element model of the laminate

To efficiently deal with different loading conditions and PV module geometries, the global coarse-scale finite element model used to simulate the structural response of the PV module should be as general as possible. To deal with the most complex loading scenario, we propose to use linear brick elements for thermo-mechanical loading simulations, or solid shell

elements like those used in [10,11]. Alternatively, if geometry and loading allow a simplification, like in case of bending of the whole PV module with respect to one of its two symmetry axes, it might be convenient to consider a cross-section of the module and perform a 2D simulation using two-dimensional linear continuum elements. Examples will be provided in Section 4.

In any case, solid-like discretizations (2D plane stress or plane strain solid elements for plane problems; bricks and tetrahedra, or solid shell finite elements for three dimensional problems) should be preferred over Kirchhoff–Love plate elements used in [7] for the following reasons:

- In the framework of solid-like finite elements it is easier to accurately model the interspace between solar cells than in Kirchhoff plate elements. This task is important when the evolution of the gap between solar cells is a quantity of interest, viz. for the prediction of failure of the busbars due to cyclic thermo-mechanical loads.
- Thermo-visco-elastic constitutive models for the encapsulant are easier to be implemented in solid-like elements than in Kirchhoff plate elements. Generalized thermo-visco-elastic models are in fact already available in most of the commercial packages and this might foster the use of the proposed global/local approach at the industrial level for the simulation of degradation processes in PV modules [12–14].
- Solid-like finite elements have a kinematics that can be consistently coupled with 2D or 3D interface elements for cohesive fracture [11], since only translational degrees of freedom are present without rotational degrees of freedom like in the Kirchhoff plate elements. This is important for the simulation of the decohesion of the backsheet layer from the other laminae, a phenomenon requiring the discretization of all the laminae composing the PV stack. In the case of problems displaying large displacements, the interface element formulation proposed in [10,15] can also be consistently used.

From the global coarse-scale finite element model of the laminate, displacements in the x, y and z directions of the nodes of the finite elements belonging to the edges of the solar cells can be determined by a simple post-processing of the linear finite element results. These displacements have to be passed as input to the local model as boundary conditions. In doing this, since the finite element discretization used in the fine-scale model is not required to match the one used in the global model, a projection operation has to be programmed. From the algorithmic point of view, it is convenient to introduce geometrical entities like facets to distinguish between the nodes of the finite elements belonging to the different sides of the solar cell, namely the lower side, the upper side, the two vertical sides along the x-direction, and the two vertical sides along the y-direction.

For each node of the finite elements belonging to a given facet of the local model, their displacement boundary conditions are evaluated by performing a linear interpolation between the displacement values of the closest neighboring nodes in the global model. This projection procedure is described in the Algorithm 1.

Algorithm 1. Numerical algorithm for the displacements projection from the global to the local model.

for $t = 1$ **to** T displacement or loading increments **do**
  Impose force or displacement boundary conditions in the global model;
  Solve the global model in terms of displacements using a full Newton–Raphson method in case of nonlinear constitutive laws for cohesive interfaces between the layers, or for geometric nonlinearities, if included;
  for $s = 1$ **to** S solar cells **do**
    for $i = 1$ **to** N facets defining the sides of the cell **do**
      for $j = 1$ **to** M nodes in the local model belonging to the facet i **do**
        Find the two closest nodes P_1 and P_2 belonging to the same facet in the global model;
        Impose a displacement vector $\mathbf{u}_j = N_1\mathbf{u}^{(1)} + N_2\mathbf{u}^{(2)}$, where $\mathbf{u}^{(1)}$ and $\mathbf{u}^{(2)}$ are the displacement vectors of the nodes P_1 and P_2, and N_k are linear shape functions $(k = 1, 2)$.
      end
    end
  end
end

2.2. The fine-scale finite element model of the solar cells

In the fine-scale model of each solar cell, a three dimensional finite element discretization of the continuum is considered by using linear brick elements. A MATLAB pre-processor for the finite element analysis program FEAP [16] has been written to generate the finite element mesh of monocrystalline Silicon solar cells including one or two internal cracks, whose locations are defined by the coordinates of their tips. Block commands in FEAP are used to generate a structured finite element mesh and duplicate the nodes of the elements along the crack. Three dimensional interface elements with a cohesive zone model formulation are then inserted through the cell thickness with a certain traction-separation relation that can be defined arbitrarily. An example of a 3D finite element discretization of a solar cell is shown in Fig. 5.

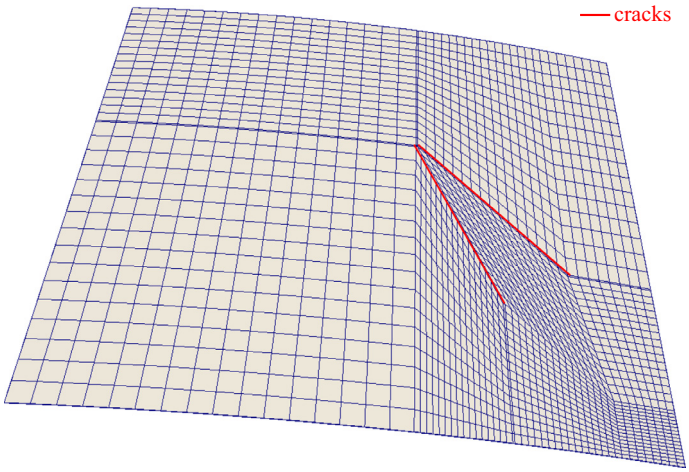

Fig. 5. An example of a local model with two cohesive cracks in red. (For interpretation of the references to colour in this figure legend, the reader is referred to the web version of this article.)

Since the interface elements are the only elements inducing a nonlinearity in the local model, their modeling is herein presented with care. The contribution to the Principle of Virtual Work of the interface cohesive tractions $\mathbf{T}$ acting along the cohesive crack surfaces S_0 is:

$$\Pi_{\text{crack}} = \int_{S_0} \mathbf{g}_{\text{loc}}^{\text{T}} \mathbf{T}\, \mathrm{d}S \tag{1}$$

where $\mathbf{g}_{\text{loc}}$ is the gap vector that accounts for opening and sliding displacements between the two faces of the crack. The virtual variation of Π_{crack} reads:

$$\delta\Pi_{\text{crack}} = \delta\mathbf{u}^{\text{T}} \int_{S_0} \left(\frac{\partial \mathbf{g}_{\text{loc}}}{\partial \mathbf{u}}\right)^{\text{T}} \mathbf{T}\, \mathrm{d}S \tag{2}$$

Introducing now the discretization of the interface by using isoparametric finite elements, the interpolated position vector of the points belonging to the average plane between the crack faces in the undeformed configuration is obtained by multiplying the interface element nodal values by the operator $\mathbf{N}$ that collects the shape functions:

$$\overline{\mathbf{X}} \cong \overline{\mathbf{X}}^e = \mathbf{N}\mathbf{M}\mathbf{X}^n, \tag{3}$$

where the superscript n denotes quantities evaluated at the nodes of the discretized geometry, viz. $\mathbf{X}^n = (X_1, Y_1, Z_1 \ldots, X_8, Y_8, Z_8)^{\text{T}}$. In case of a 3D quadrilateral linear interface element (see Fig. 6), the matrix operators have the following expression:

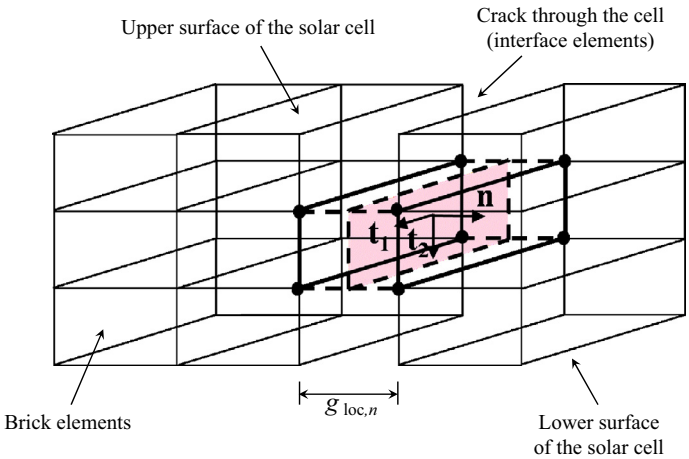

Fig. 6. A sketch of an interface element embedded between brick elements, through the thickness of Silicon cells.

$$\mathbf{N} = [N_1\mathbf{I} \quad N_2\mathbf{I} \quad N_3\mathbf{I} \quad N_4\mathbf{I}] \tag{4a}$$

$$\mathbf{M} = \frac{1}{2}\begin{bmatrix} \mathbf{I} & \mathbf{0} & \mathbf{0} & \mathbf{0} & \mathbf{I} & \mathbf{0} & \mathbf{0} & \mathbf{0} \\ \mathbf{0} & \mathbf{I} & \mathbf{0} & \mathbf{0} & \mathbf{0} & \mathbf{I} & \mathbf{0} & \mathbf{0} \\ \mathbf{0} & \mathbf{0} & \mathbf{I} & \mathbf{0} & \mathbf{0} & \mathbf{0} & \mathbf{I} & \mathbf{0} \\ \mathbf{0} & \mathbf{0} & \mathbf{0} & \mathbf{I} & \mathbf{0} & \mathbf{0} & \mathbf{0} & \mathbf{I} \end{bmatrix} \tag{4b}$$

where $\mathbf{0}$ is a 3×3 null matrix and $\mathbf{I}$ is a 3×3 identity matrix. The shape functions in the standard natural reference system $(s_1, s_2) \in [-1, +1] \times [-1, +1]$ read:

$$N_1 = \frac{1}{4}(1 - s_1)(1 - s_2) \tag{5a}$$

$$N_2 = \frac{1}{4}(1 + s_1)(1 - s_2) \tag{5b}$$

$$N_3 = \frac{1}{4}(1 + s_1)(1 + s_2) \tag{5c}$$

$$N_4 = \frac{1}{4}(1 - s_1)(1 + s_2) \tag{5d}$$

The gap vector in the reference cartesian frame, $\mathbf{g}$, can be obtained by pre-multiplying the nodal displacement vector $\mathbf{d} = (u_1, v_1, w_1 \ldots, u_8, v_8, w_8)^{\mathrm{T}}$ by a suitable operator $\mathbf{L}$ which provides the difference between the displacements of the two crack faces. Within the finite element discretization, the interpolation scheme of the gap vector reads:

$$\mathbf{g} \cong \mathbf{g}^e = \mathbf{NLd} \tag{6}$$

where the matrix operator $\mathbf{L}$ is:

$$\mathbf{L} = \begin{bmatrix} -\mathbf{I} & \mathbf{0} & \mathbf{0} & \mathbf{0} & \mathbf{I} & \mathbf{0} & \mathbf{0} & \mathbf{0} \\ \mathbf{0} & -\mathbf{I} & \mathbf{0} & \mathbf{0} & \mathbf{0} & \mathbf{I} & \mathbf{0} & \mathbf{0} \\ \mathbf{0} & \mathbf{0} & -\mathbf{I} & \mathbf{0} & \mathbf{0} & \mathbf{0} & \mathbf{I} & \mathbf{0} \\ \mathbf{0} & \mathbf{0} & \mathbf{0} & -\mathbf{I} & \mathbf{0} & \mathbf{0} & \mathbf{0} & \mathbf{I} \end{bmatrix} \tag{7}$$

The constitutive relation for the crack, i.e., the so-called cohesive zone model (CZM), is usually provided in a local frame defined by the tangential and the normal vectors to the middle surface of the interface element ($\mathbf{t}_1, \mathbf{t}_2$ and $\mathbf{n}$), see Fig. 6. These unit vectors can be determined via differentiation of the average coordinates with respect to the natural coordinates s_1 and s_2.

The gap vector in this local frame, $\mathbf{g}_{\mathrm{loc}} = (g_{\mathrm{loc},t_1}, g_{\mathrm{loc},t_2}, g_{\mathrm{loc,n}})^{\mathrm{T}}$, is computed by multiplying the gap vector in the reference frame by a rotation operator $\mathbf{R}$:

$$\mathbf{g}^e_{\mathrm{loc}} = \mathbf{R}\mathbf{g}^e \tag{8}$$

where the rotation matrix collects the components of the unit vectors $\mathbf{t}_1, \mathbf{t}_2$, and $\mathbf{n}$:

$$\mathbf{R} = \begin{bmatrix} t_{1,x} & t_{1,y} & t_{1,z} \\ t_{2,x} & t_{2,y} & t_{2,z} \\ n_x & n_y & n_z \end{bmatrix} \tag{9}$$

Introducing the finite element discretization, Eq. (8) can be rephrased as:

$$\mathbf{g}^e_{\mathrm{loc}} = \mathbf{RNLd} = \mathbf{RBd} \tag{10}$$

where $\mathbf{B} := \mathbf{NL}$ has been introduced to simplify the notation. Examining the terms entering the virtual variation of Eq. (2), the partial derivative $(\partial \mathbf{g}_{\mathrm{loc}}/\partial \mathbf{u})$ is given by:

$$\frac{\partial \mathbf{g}_{\mathrm{loc}}}{\partial \mathbf{u}} \cong \frac{\partial \mathbf{g}^e_{\mathrm{loc}}}{\partial \mathbf{d}} = \mathbf{RB} \tag{11}$$

Inserting this intermediate result into the discretized version of Eq. (2), where $\mathbf{u}$ is simply replaced by $\mathbf{d}$, the following general formulation valid for any CZM relation is derived:

$$\delta\Pi^e_{\mathrm{crack}} = \delta\mathbf{d}^{\mathrm{T}} \int_{S_0} (\mathbf{RB})^{\mathrm{T}}\mathbf{T}\,\mathrm{d}S \tag{12}$$

For the cohesive traction vector $\mathbf{T} = (\tau_1, \tau_2, \sigma)^{\mathrm{T}}$, an irreversible CZM whose shape is characterized by a linear ascending branch followed by an exponential softening is used. Coupling between fracture modes is accounted for. The resulting expressions for the normal and total tangential cohesive tractions are:

$$\sigma = \begin{cases} \sigma_{\max} \exp\left(\frac{-l_0-|g_t|}{r}\right)\frac{g_n}{l_0}, & \text{if} \quad 0 \leqslant \frac{g_n}{r} < \frac{l_0}{r} \\ \sigma_{\max} \exp\left(\frac{-g_n-|g_t|}{r}\right), & \text{if} \quad \frac{l_0}{r} \leqslant \frac{g_n}{r} < \frac{g_{nc}}{r} \\ 0, & \text{if} \quad \frac{g_n}{r} \geqslant \frac{g_{nc}}{r} \end{cases} \tag{13}$$

$$\tau = \begin{cases} \tau_{\max} \exp\left(\frac{-l_0-g_n}{r}\right)\frac{g_t}{l_0}, & \text{if} \quad 0 \leqslant \frac{|g_t|}{r} < \frac{l_0}{r} \\ \tau_{\max}\,\mathrm{sgn}(g_t) \exp\left(\frac{-g_n-|g_t|}{r}\right), & \text{if} \quad \frac{l_0}{r} \leqslant \frac{|g_t|}{r} < \frac{g_{tc}}{r} \\ 0, & \text{if} \quad \frac{|g_t|}{r} \geqslant \frac{g_{tc}}{r} \end{cases} \tag{14}$$

where the model parameters are: l_0, which defines the opening and sliding displacements corresponding to the peak CZM tractions before the onset of exponential softening; the critical opening and sliding displacements, g_{nc} and g_{tc}, corresponding to complete debonding in pure opening and shearing loading; the root mean square of the microscopic surface roughness of the crack profile, r, computed as in [8]. As compared to other CZM formulations like in [22], defining the cohesive tractions by a single nonlinear equation over the whole separation range which is easier to be numerically implemented, here the ascending branch is treated separately from the softening one. This choice allows us to keep the slope of the linear branch high and not related to the value of $\sigma_{\max}$, and keep constant the interface fracture energy acting on g_{nc} and g_{tc}. A graphical representation of the pure Mode I and Mode II CZM relations is provided in Fig. 7.

Due to the nonlinearity in the CZM relation, a consistent linearization of Eq. (12) is required for the application of the Newton–Raphson solution scheme. The contribution of the weak form at the $k+1$ iteration can be related to that of the previous iteration k by a truncated Taylor series expansion:

$$\delta\Pi^e_{\text{crack}}(\mathbf{d}^{k+1}) \cong \delta\Pi^e_{\text{crack}}(\mathbf{d}^{k}) + \frac{\partial \delta\Pi^e_{\text{crack}}(\mathbf{d}^{k})}{\partial \mathbf{d}}\Delta\mathbf{d} \tag{15}$$

where $\Delta\mathbf{d} = \mathbf{d}^{k+1} - \mathbf{d}^{k}$. Henceforth, the iteration index will be omitted to simplify notation. Performing the linearization of the cohesive traction vector $\mathbf{T} = (\tau_1, \tau_2, \sigma)^{\mathrm{T}}$ as customary, we obtain:

$$\frac{\partial \mathbf{T}}{\partial \mathbf{g}_{\text{loc}}} = \mathbf{C} \tag{16}$$

where $\mathbf{C}$ represents the tangent interface constitutive matrix of the element:

$$\mathbf{C} = \begin{bmatrix} \frac{\partial \tau_1}{\partial g_{\text{loc,t1}}} & \frac{\partial \tau_1}{\partial g_{\text{loc,t2}}} & \frac{\partial \tau_1}{\partial g_{\text{loc,n}}} \\ \frac{\partial \tau_2}{\partial g_{\text{loc,t1}}} & \frac{\partial \tau_2}{\partial g_{\text{loc,t2}}} & \frac{\partial \tau_2}{\partial g_{\text{loc,n}}} \\ \frac{\partial \sigma}{\partial g_{\text{loc,t1}}} & \frac{\partial \sigma}{\partial g_{\text{loc,t2}}} & \frac{\partial \sigma}{\partial g_{\text{loc,n}}} \end{bmatrix} \tag{17}$$

The final formulation is the following:

$$\frac{\partial \delta\Pi^e_{\text{int}}(\mathbf{d})}{\partial \mathbf{d}} = \int_{S_0} \mathbf{B}^{\mathrm{T}}\mathbf{R}^{\mathrm{T}}\mathbf{C}\mathbf{R}\mathbf{B}\,\mathrm{d}S \tag{18}$$

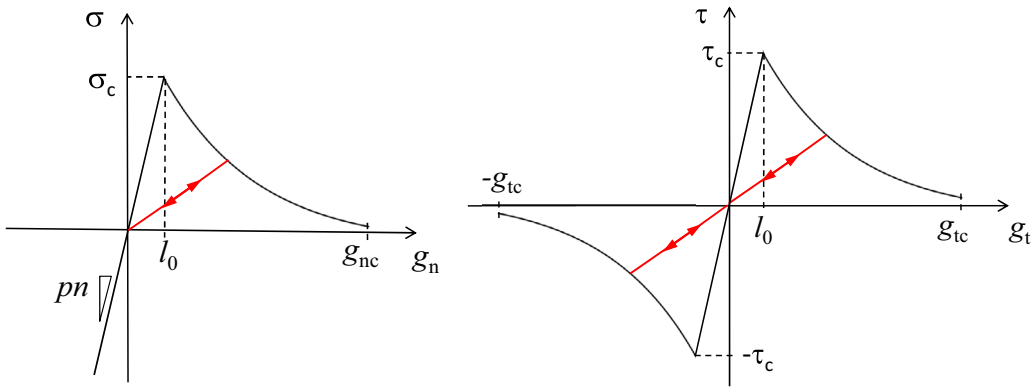

(a) Mode I (b) Mode II

Fig. 7. CZM formulation for irreversible opening and sliding deformation.

providing the residual vector $\mathbf{f}_{\text{crack}}$ and the tangent stiffness matrix $\mathbf{K}$ of the interface element:

$$\mathbf{f}_{\text{crack}} = \int_{S_0} (\mathbf{RB})^{\mathrm{T}} \mathbf{T}\, \mathrm{d}S \tag{19a}$$

$$\mathbf{K} = \int_{S_0} \mathbf{B}^{\mathrm{T}} \mathbf{R}^{\mathrm{T}} \mathbf{C} \mathbf{R} \mathbf{B}\, \mathrm{d}S \tag{19b}$$

This formulation can also be augmented by considering thermal conduction as proposed for 2D in [8]. The crack opening displacement computed at each node of the interface element is finally passed as input to the electric model, which allows for the simulation of the electric response of the solar cell.

3. The electric model

The most common PV solar cells are made of Silicon. An atom of Silicon in the crystal lattice absorbs a photon of the incident solar radiation and, if the energy of the photon is high enough, then an electron from the outer shell of the atom is freed. This process results in the formation of a hole-electron pair, where the hole is a place where there is a lack of an electron in the crystal structure. To avoid the natural recombination of electrons and holes, a potential barrier is built into the cells by doping the Silicon on the side exposed to sunlight with Phosphorous, to form *n*-Silicon, which has an excess of electrons in its outer shell. Similarly, on the opposite side, Silicon is doped with a very small amount of Boron, to form *p*-Silicon, which has a deficiency of electrons in its outer shell. By connecting the $p-n$ junction via an external circuit, a current flows through it. Electrical contacts are made by metal bases on the bottom of the cell and by metal grids (fingers) on the top layer. These fingers are soldered to busbars that are the main conductors connecting in series the various solar cells building the PV module, see the sketch in Fig. 8.

Under the assumption of an ideal semiconductor, which has homogeneous properties everywhere in the plane of the solar cell, a simple one-dimensional electric model can be introduced to quantify the amount of current $I_{\mathrm{f}}(\xi)$ along the finger, for each position described by the coordinate ξ ranging from one busbar to the other. According to [17], in fact, the voltage is not constant, but it is a function of ξ due to a distributed resistance of the grid line, caused by metallization and emitter resistances. For each voltage $V(\xi)$, the current I_{tt} through the thickness of the cell, i.e., through the $p-n$ junction, can be finally modeled by a single diode equation.

In the present section, this electrical model is generalized by accounting for one or two intersecting cracks. Preliminary results in [18] have shown that, in addition to the spatial variation of the grid line resistance as in [17], a localized resistance at the position along the finger crossed by a crack has to be introduced to model experimental trends. However, the relation between this localized resistance and the crack opening was not investigated in [18] and is the subject of the present study.

By introducing for each finger a local reference frame (ξ, η, ζ) with the axis ξ directed along the finger direction and ranging from the first busbar at $\xi = 0$ to the second at $\xi = l$ (see Fig. 8), the surface density of electric current through the thickness of the solar cell originated in the semiconductor by the photovoltaic effect, I_{tt} (A/cm^2), the voltage V (V), and the linear density of current (per unit depth) along the finger, I_{f} (A/cm), depend on the position ξ due to the sheet resistance in the ξ-direction ρ_{S} (Ω/cm^2) evaluated as the grid resistance R_{grid} (Ω/cm) divided by the spacing between two fingers.

Without illumination from the sun, as during the conditions of the electroluminescence test performed inside a dark room, where the voltage at the busbars is externally imposed by a power supplier, the following ordinary differential equation relates the linear density of current along the finger $I_{\mathrm{f}}(\xi)$ to the derivative of the voltage:

$$\frac{\mathrm{d}V(\xi)}{\mathrm{d}\xi} = -\rho_{\mathrm{S}} I_{\mathrm{f}}(\xi) \tag{20}$$

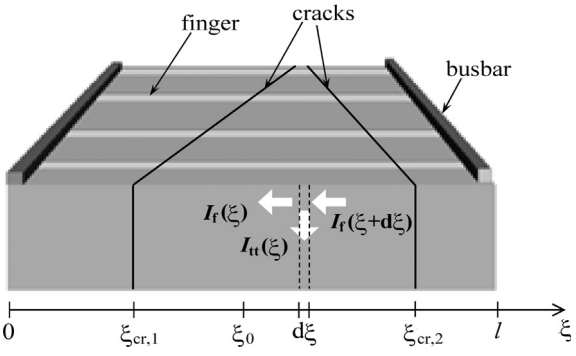

Fig. 8. Schematic representation of a finger intersected by two cracks.

Moreover, for continuity conditions on an infinitesimal portion of the grid line and the solar cell behind it, the derivative of the linear density of current along the finger has to be equal to the surface density of current passing through the solar cell thickness:

$$\frac{\mathrm{d}I_{\mathrm{f}}(\xi)}{\mathrm{d}\xi} = -I_{\mathrm{tt}}(\xi) \tag{21}$$

By inserting the expression for I_{f} in Eq. (20) into Eq. (21), the following second order ordinary differential equation is derived:

$$\frac{\mathrm{d}^2V(\xi)}{\mathrm{d}\xi^2} = \rho_{\mathrm{S}} I_{\mathrm{tt}}(\xi) \tag{22}$$

The surface density of current through the thickness of the solar cell, I_{tt}, is due to the semiconductor properties whose response can be approximated by a single diode model [7]:

$$I_{\mathrm{tt}}(\xi) = I_{01} \exp\left(\frac{V(\xi) - R_{\mathrm{hom}} I_{\mathrm{tt}}(x)}{n_1 V_T}\right) \tag{23}$$

where R_{hom} is the local sheet resistance in series with the diode, I_{01} is the saturation current density, $n_1 \sim 1$ is the ideality factor, $V_{\mathrm{T}} = kT/e$ is the thermal voltage dependent on the absolute temperature T and on the Boltzmann's constants k and e, the magnitude of the electrical charge of the electron.

Due to the implicit nature of Eq. (23), the current I_{tt} cannot be obtained in a closed form and we suggest to recast Eq. (23) in a way so that the Newton–Raphson method can be applied:

$$f(I_{\mathrm{tt}}(\xi)) = I_{\mathrm{tt}}(\xi) - I_{01} \exp\left(\frac{V(\xi) - R_{\mathrm{hom}} I_{\mathrm{tt}}(\xi)}{n_1 V_T}\right) = 0 \tag{24}$$

The approximation $I_{\mathrm{tt}}^{i+1}(\xi)$ at a generic iteration $i+1$ is obtained from that of the previous iteration $I_{\mathrm{tt}}^{i}(\xi)$ as follows:

$$I_{\mathrm{tt}}^{i+1}(\xi) = I_{\mathrm{tt}}^{i}(\xi) - \left[\frac{\mathrm{d}f}{\mathrm{d}I_{\mathrm{tt}}}\right]_i^{-1} f(I_{\mathrm{tt}}^{i}(\xi)) \tag{25}$$

where:

$$\left[\frac{\mathrm{d}f}{\mathrm{d}I_{\mathrm{tt}}}\right]_i = 1 + I_{01} \exp\left(\frac{V(\xi) - R_{\mathrm{hom}} I_{\mathrm{tt}}^{i}(\xi)}{n_1 V_T}\right) - \frac{R_{\mathrm{hom}}}{n_1 V_T} \tag{26}$$

Considering $I_{\mathrm{tt}}^{0} = 0.2\ \mathrm{mA/cm^2}$ as the starting value, convergence is achieved when the error in the computed I_{tt} is less than a prescribed tolerance. Due to the consistent update of the tangent, the rate of convergence is quadratic and few iterations are needed to achieve an error within the machine precision.

Numerical integration of the ODE in Eq. (22) is performed by discretizing the grid line in nodes (*nnd*) with a regular spacing $\mathrm{d}\xi$. The starting point for the integration is the point at $\xi = \xi_0$ where the voltage is minimum, V_0. For a finger not intersected by cracks, this point is simply located in the middle between two busbars ($\xi_0 = l/2$). For a finger intersected by a crack, ξ_0 is a free parameter to be identified by matching the value of the voltage at the busbars, which is a known imposed value in the EL test (see the sketch in Fig. 8). For a tentative value of ξ_0, whose initial guess can be $\xi_0 = l/2$ and the corresponding voltage, $V(\xi_0) = V_0$, which is in general lower than the applied voltage at the level of busbars (0.7 V for a typical EL test), the integration path is separated in two parts. In reference to Fig. 8, the first part is comprised between ξ_0 and the busbar on the left, and the second part ranges from ξ_0 and the busbar on the right. The current density $I_{\mathrm{tt}}(\xi)$ is assumed to be constant within each integration interval. Under such an hypothesis, the voltage profile within each interval $\mathrm{d}\xi$ is parabolic and the following equations hold:

$$V(\xi + \mathrm{d}\xi) = V(\xi) + V'(\xi)\mathrm{d}\xi + \frac{1}{2}V''(\xi)\mathrm{d}\xi^2 \tag{27a}$$

$$V'(\xi + \mathrm{d}\xi) = V'(\xi) + V''(\xi)\mathrm{d}\xi \tag{27b}$$

$$I_{\mathrm{f}}(\xi + \mathrm{d}\xi) = I_{\mathrm{f}}(\xi) + I_{\mathrm{tt}}(\xi)\mathrm{d}\xi \tag{27c}$$

where $(')$ and $('')$ denote, respectively, first and second order derivatives with respect to ξ.

Examining the integration in the first region (from $\xi = \xi_0$ to $\xi = 0$), the boundary conditions are $V(\xi_0) = V_0$ and $V'(\xi_0) = 0$. The vertical current $I_{\mathrm{tt}}(\xi)$ is then computed with the Newton–Raphson method applied to Eq. (23). Next step, the voltage $V(\xi - \mathrm{d}\xi)$, its derivative $V'(\xi - \mathrm{d}\xi)$ and the linear density of current along the finger, $I_{\mathrm{f}}(\xi - \mathrm{d}\xi)$ are evaluated at the new integration point $\xi - \mathrm{d}\xi$ according to Eq. (27). The negative sign of $\mathrm{d}\xi$ is due to the fact that we are integrating from $\xi = \xi_0 > 0$ to $\xi = 0$.

At the point $\xi_{\mathrm{cr},1}$ where a crack crosses the finger, an additional localized resistance $R_{\mathrm{cr},1}$ is introduced, dependent on its crack opening, in agreement with experimental findings in [19] recently confirmed by optical microscope images and electric measurements in [20]. Indeed, as firstly pointed out in [19], the effect of a crack on I_{tt} is quite evident from the analysis of EL

images. The brightness of the EL image, in fact, is proportional to I_{tt} [21] by a scaling factor. When the crack opening displacement is sufficiently large, a discontinuity in the gray-scale of the EL image takes place. Due to the presence of the concentrated resistance, a discontinuity in the voltage distribution takes place in correspondence of this crack position, $\xi_{cr,1}$:

$$V(\xi_{cr,1}^{-}) = V(\xi_{cr,1}^{+}) + R_{cr,1} I_f(\xi_{cr,1}) \tag{28}$$

Afterwards, the integration proceeds as previously done before meeting the crack. Regarding the integration in the second region, from $\xi = \xi_0$ up to $\xi = l$, the same procedure as before is applied to compute $V(\xi + d\xi)$, $V'(\xi + d\xi)$ and $I_f(\xi + d\xi)$ in the point with coordinate $\xi + d\xi$, starting from the boundary condition imposed at $\xi = \xi_0$.

Again, in case of another crack intersecting the finger at $\xi = \xi_{cr,2}$, the voltage is increased in that point by the action of a concentrated resistance $R_{cr,2}$. The algorithm for two cracks intersecting a finger, which is the most general case found from EL inspections after production, is summarized in Algorithm 2. In the case of a single crack, it is sufficient to set equal to zero one of the two localized crack resistances.

Algorithm 2. Algorithm for the computation of the electric voltage and currents along a finger intersected by one or two cracks.

Data: $d\xi, \xi_{cr,1}, \xi_{cr,2}$; number of integration points nnd_1 and nnd_2; distance l between two busbars; tolerance $tol_0 = 5 \times 10^{-2}$ on the error w.r.t. experimental data; tolerance $tol_1 = 0.7/10$ w.r.t. the value of the voltage at the busbars, V_b spatial tolerance $tol_2 = l/\max\{nnd_1, nnd_2\}$; tolerance $tol_3 = 1 \times 10^{-13}$ of the Newton–Raphson method
Initialize: norm $\leftarrow 1$, $norm_V \leftarrow 1$, error $\leftarrow 1$, $error_V \leftarrow 1$, $V_0 \leftarrow 0.7$, $\xi_0 \leftarrow l/2$
while error $> tol_0$ **do**
  while $error_V > tol_1$ **do**
    Integrate from $\xi = \xi_0$ to $\xi = 0$:
    for $j = 1$ **to** nnd_1 **do**
      if $|\xi - \xi_{cr,1}| < tol_2$ **then**
        Modify the voltage V according to Eq. (28)
      end
      Compute $I_{tt,j}$ with the Newton–Raphson method;
      Initialize $i = 1, I_{tt}^i = 0.2$ A;
      while norm $> tol_3$ **do**
        $i \leftarrow i + 1$;
        Compute I_{tt}^i, Eq. (25);
        Compute norm $= \|I_{tt}^i - I_{tt}^{i-1}\|$
      end
      $I_{tt,j} \leftarrow I_{tt}^{i+1}$;
      Compute $I_{f,j}, V_j''$, and V_j' using Eq. (27), $\xi \leftarrow \xi - d\xi$
    end
    Integrate from $\xi = \xi_0$ to $\xi = l$:
    for $j = 1$ **to** nnd_2 **do**
      if $|\xi - \xi_{cr,2}| < tol_2$ **then**
        Modify the voltage V according to Eq. (28)
      end
      Compute $I_{tt,j}$ with the Newton–Raphson method;
      Initialize $i = 1, I_{tt}^i = 0.2$ A;
      while error$>tol_3$ **do**
        $i \leftarrow i + 1$; Compute I_{tt}^i, Eq. (25);
        Compute norm $= \|I_{tt}^i - I_{tt}^{i-1}\|$;
      end
      $I_{tt,j} \leftarrow I_{tt}^{i+1}$;
      Compute $I_{f,j}, V_j''$, and V_j' using Eq. (27), $\xi \leftarrow \xi + d\xi$;
    end
    Compute $error_V = \max\{\|V(\xi = 0) - V_b\|, \|V(\xi = l) - V_b\|\}$ and modify ξ_0;
  end
  Compute error$= \sum_{k=1}^{nnd_1+nnd_2} (I_{tt}^k - I_{exp}^k)/I_{exp}^k$ and reduce V_0;
end

4. Model parameters identification

4.1. Description of the experimental test

To get insight into the mechanisms leading to the coupling between the mechanical and the electric fields due to cracks and identify the model parameters, a bending test on a rectangular PV module was performed by monitoring cracking at different deformation levels by using EL imaging. This is a non-destructive method based on the evaluation of the level of luminescence emitted by Silicon when subjected to an imposed electric potential in forward bias condition. Electrically insulated zones or cracks can be identified by their low EL intensity, thus resulting in dimmer images. In the present tests, a voltage of 0.7 V was applied to the PV panels by the Genesys GENH60-12.5 (750W-1U, TDK Lambda) power supplier. EL emission was detected by the cooled digital 12 bit CCD camera pco.1300 solar, with a resolution of 1392×1040 pixel and equipped by the Schneider Kreuznach XNP F1.4 lens with SWIR coating 800–1800 nm. Tests were performed inside a darkroom, shading all the possible sources of light to avoid reflection effects. By using nearly the maximum aperture of the camera (F1.8), the focus of the camera was adjusted during the bending test to obtain perfect focus for all the various deflections of the module. An exposure time of 5 s was used for each photo. A post-processing of the acquired EL images was made by using the facilities of the software CamWare. In particular, cut-off filters of 600 and 8200 nm were used for all the images to make them comparable and remove very high and very low emission in the spectrum of the signal. EL data at any pixel can be converted in current through the thickness, I_{tt}, according to the method proposed in [21].

A semi-flexible module made of 2 rows of 5 monocrystalline Silicon solar cells each was tested in bending. The size of the cells is 156×156 mm. The partially symmetric arrangement of the layers through the thickness (0.265 mm of polyethylene terephthalate, 0.600 mm of epoxy-vinyl-acetate, 0.166 mm of Silicon, 0.400 mm of epoxy-vinyl-acetate and 0.345 mm of backsheet, see Fig. 2(b)) and the different Young moduli of the materials lead to Si cells just above the neutral axis of the cross-section. This type of module, which has a certain degree of flexibility, can be used in many applications where the substrate to be bonded is curved. In order to induce a tensile stress state inside solar cells, the curvature imposed to the module was such that the convex side after bending corresponds to the PET side (front side, see Fig. 9).

To create pre-existing cracks and study their evolution depending on the imposed bending, moderate impacts were made with PMMA balls of 4 cm of diameter at a velocity of 6 m/s, simulating the action of hail impacts. In this way, cracks are introduced by an indentation effect. The PV module is then loaded in bending and the EL images of the four solar cells in the middle of the panel are shown in Fig. 10 for different mid-span deflections. Location of impacts can be clearly distinguished by the circular dark spots from where diagonal cracks, influenced by the crystallographic planes of cubic face centered monocrystalline Silicon, depart. These patterns are completely invisible with the naked eye and can only be determined by the EL technique.

In the sequel, as far as the numerical model is concerned, we focus our attention on the cell No. 1, which has a crack between two busbars near the left edge of the cell far from the other cracks. Its local electric resistance is increasing with deflection, as it can be seen by the localized dimmer EL signal around the crack.

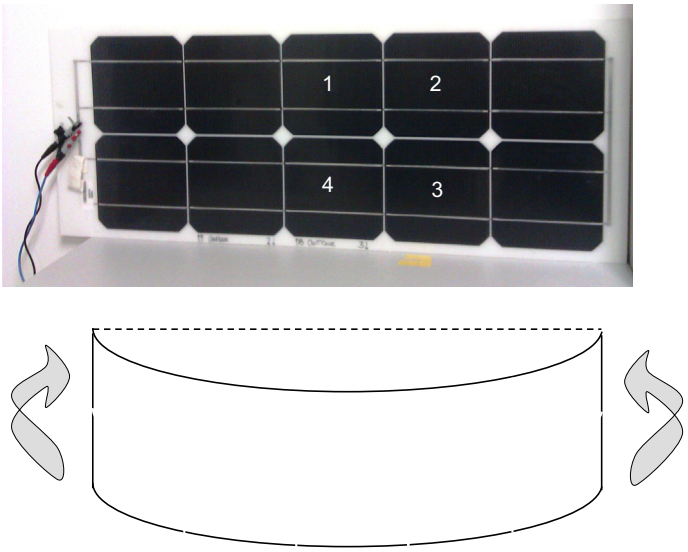

Fig. 9. Sketch of the mechanical test. The cells 1–4 are monitored by EL and their images are shown in Fig. 10.

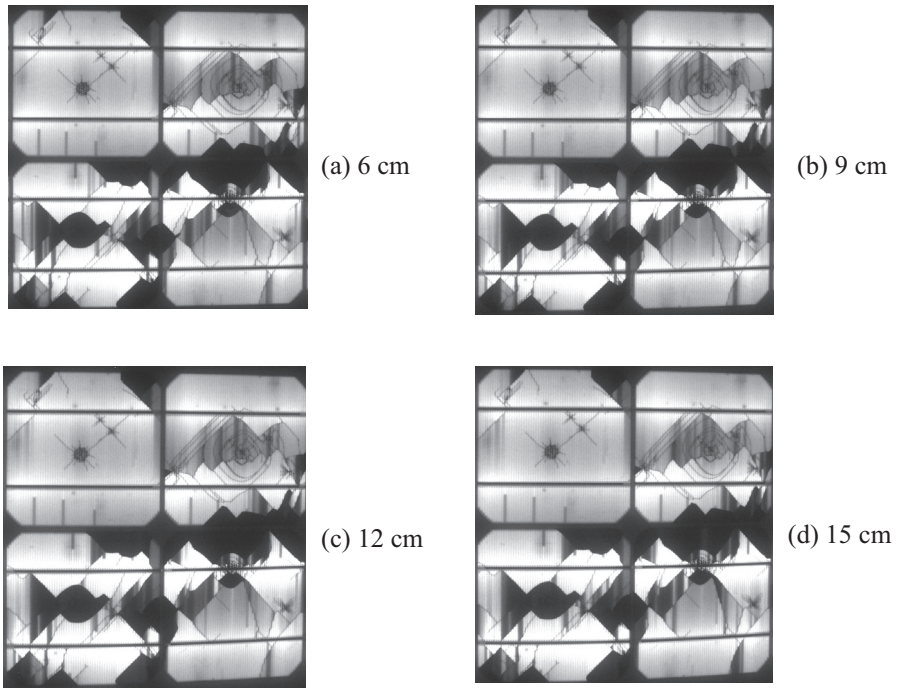

Fig. 10. Electroluminescence images of the 4 solar cells in Fig. 9, for different deflections of the PV module.

4.2. Description of the numerical simulation

The well defined geometry of the test and the application of a mono-axial bending allow the use of the coarse-scale analysis for a single cross-section of the module, parallel to the bending plane. Therefore, a 2D plane strain model has been considered, in which the layers of the module are explicitly represented, with their specific mechanical and geometrical parameters. Furthermore, the symmetry of the problem can be exploited in order to analyze only half the module, as shown in Fig. 11(a). In the same figure, the mesh adopted, constituted by 4-node isoparametric finite elements, is also shown. At this scale, a linear elastic behavior has been assumed for all the materials composing the layers. The visco-elastic behavior typical of EVA is not taken into account, since only short term loading at a constant ambient temperature is imposed during this test.

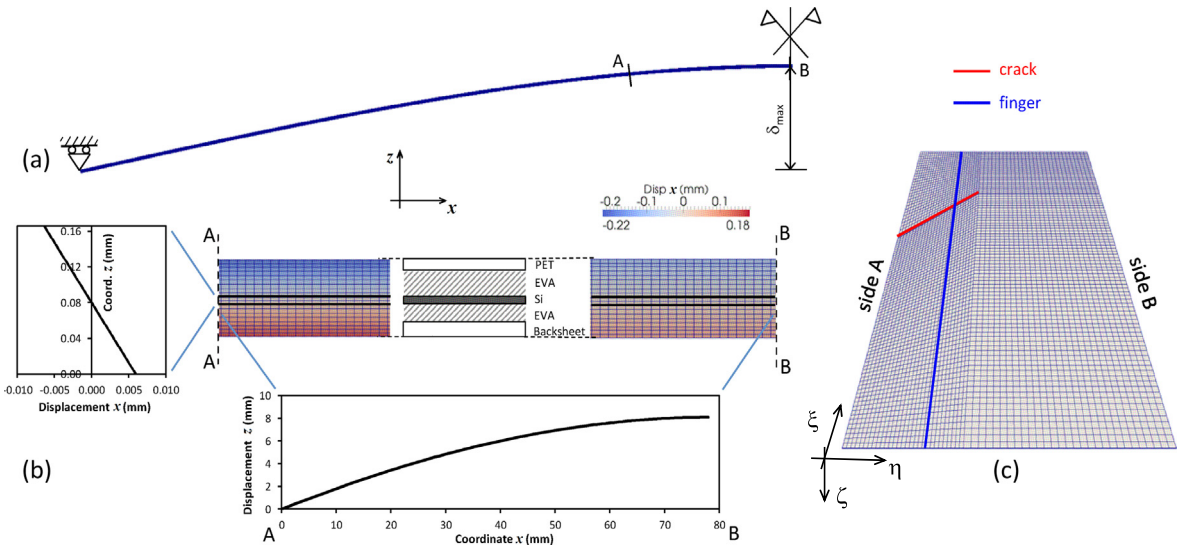

Fig. 11. (a) The coarse-scale 2D finite element model of the PV module subjected to bending; (b) displacements passed to the local model of the solar cell located between points A and B (cell number 1 in Figs. 9 and 10); (c) mesh of the local 3D finite element model of the solar cell.

The mechanical properties used are reported in Table 1. As regards the boundary conditions, the vertical displacement is restrained at the free edge, whereas symmetry boundary constraints are applied along the symmetry cross-section. Then, a transversal displacement, which corresponds to the mid-span deflection of the experimental tests, is applied in the same cross-section (see Fig. 11). For each of the considered values of deflection, namely 6, 9, 12 and 15 cm, the displacements along the boundaries of the solar cells are extracted, and used as input for the local-scale analysis as described in Sec. 2. Finite element results for the solar cell No. 1 in Fig. 9, whose EL images are shown in Fig. 10, are presented.

With reference to the coarse-scale FE model represented in Fig. 11(a), the region A-B consists of the location of the half cell investigated in the local model. A schematic of the displacements obtained along the boundaries of the cell for a given value of mid-span deflection is shown in Fig. 11(b): the left side of the cell is subjected to a linear variation of the displacement in the x-direction, whereas the top and bottom surfaces are subjected to a nonlinear displacement distribution in the z-direction, according to the deformation of the whole module. The cross-section B-B has constrained displacements along the x-direction, for symmetry reasons.

According to the procedure described in Section 2, the displacements along the boundaries are passed to the local fine-scale model as boundary conditions imposed to the nodes belonging to the various facets of the cell. At this level, a 3D finite element model with 8-node isoparametric brick elements is considered as shown in Fig. 11(c). The crack observed near the left edge of the solar cell No. 1 between the busbars in the EL test in Fig. 10 is introduced in the model before the generation of the 3D mesh, and it is discretized by interface elements described in Section 2.2. Other cracks are not modeled, since they are far apart from the considered one and their interaction is expected to be negligible. A linear elastic behavior is assumed for Silicon, with mechanical properties reported in Table 1. The cohesive zone model outlined in Section 2.2 is used for modeling the nonlinear response of cracks, with parameters typical of Silicon. In particular, we selected: $\sigma_{max}=\tau_{max}=175$ MPa, $g_{nc}=g_{tc}=0.1$ μm, $r=0.035$ μm, $l_0=0.02$ μm.

The analysis at the fine-scale model has been therefore carried out for the four different imposed displacement distributions derived from the coarse-scale model in correspondence of the four mid-span deflections. The contour plot of the in plane displacement in the ξ direction is shown in Fig. 12 for the four considered cases. Such contour plots clearly evidence

Table 1
Material properties for the coarse-scale FE model.

	E (GPa)	ν
PET	2.5	0.30
EVA	0.001	0.30
Si	160	0.22
Backsheet	2.8	0.30

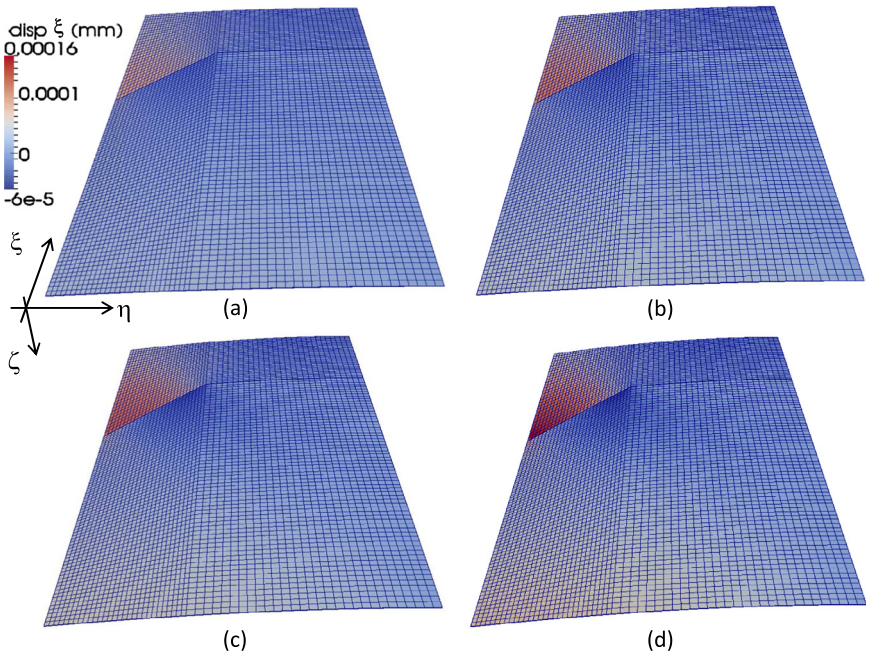

Fig. 12. Deformed meshes and contour plots of the in plane displacement in direction ξ for the 3D local fine-scale model of the cracked cell for the following values of the mid-span deflection of the module: (a) 6 cm, (b) 9 cm, (c) 12 cm, and (d) 15 cm. Note the jump of displacements in correspondence of the discontinuity represented by the crack faces.

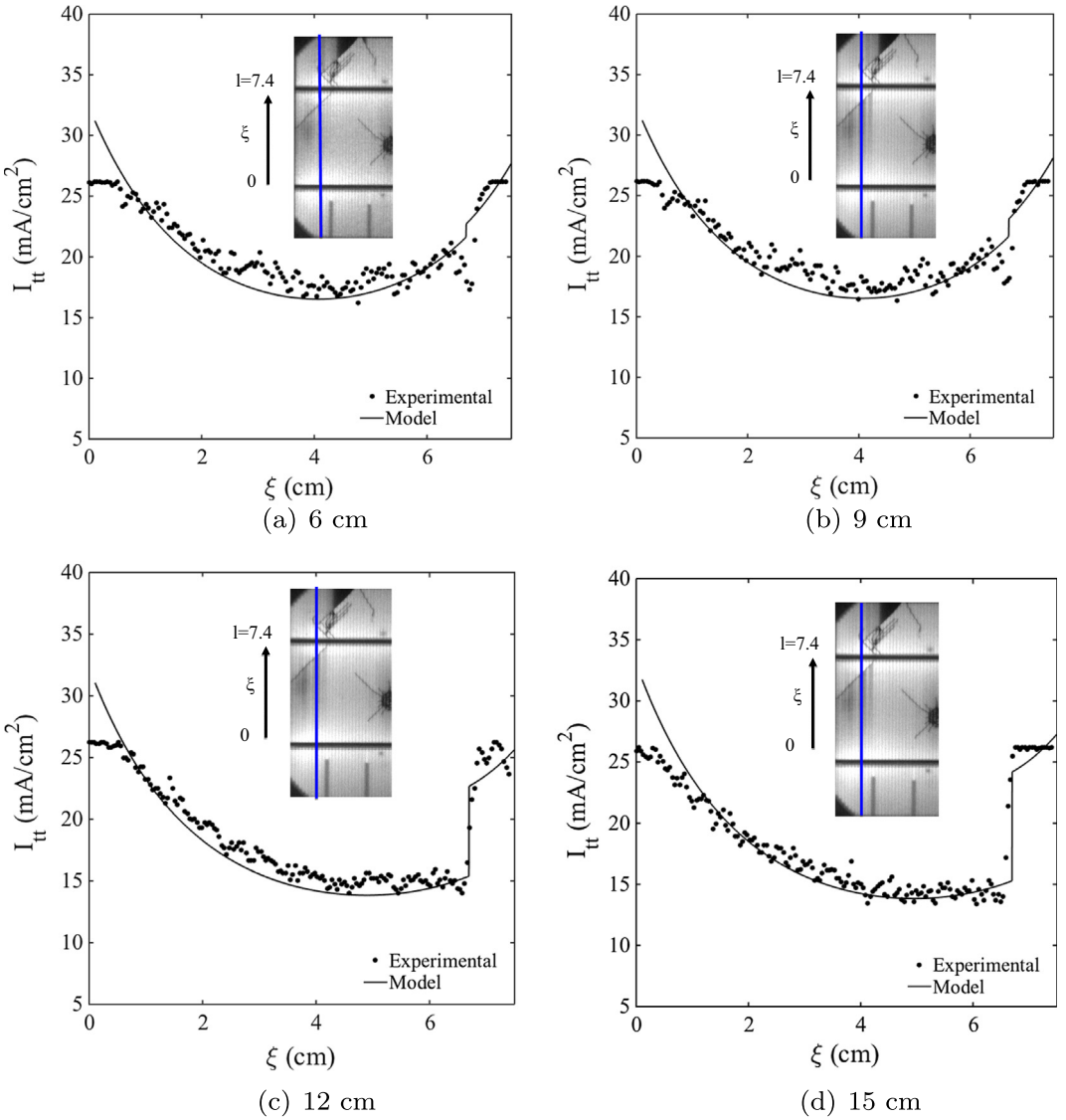

Fig. 13. Current through the cell thickness in a monocrystalline Si cell along a finger crossed by a crack for various mid-span deflections. Model parameters are reported in Table 2.

Table 2
Values of the identified parameters of the electrical model.

Deflection (cm)	g_n (μm)	ξ_0 (cm)	V_0 (V)	R_{cr} (Ω cm)
6	0.13	3.97	0.582	0.03
9	0.17	3.97	0.582	0.04
12	0.22	4.79	0.577	0.43
15	0.27	4.85	0.577	0.53

how the normal gap between the crack faces changes, which is the parameter playing the major role in determining the resistance of the crack to the electric current flux. Such a gap is an increasing function of the deflection applied to the PV module (to emphasize this correlation, the same range of colors has been selected for the four contour plots).

4.3. Identification of the relation between crack resistance and crack opening

For each deformation level, the crack opening displacement can be computed along the crack. For all the fingers, the electric model presented in Section 3 can be applied. For illustrative purposes, we focus now on a single finger crossed by the

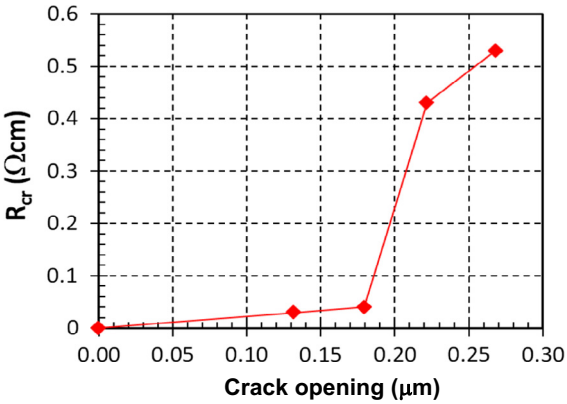

Fig. 14. Correlation between localized crack resistance and crack opening.

crack. Matching between the proposed model predictions and the experimental values of I_{tt} for different deflections allows determining the relation between crack resistance and crack opening displacement, which is the primary variable to be identified. This relationship is expected to be of general validity and independent of boundary conditions, in analogy with the cohesive zone model relating the local tractions to crack opening and sliding.

In Fig. 13 we show the predicted I_{tt} data with solid line in comparison with experimental data (in black dots). The $\xi-$coordinate ranges from 0 to $l = 7.4$ cm, i.e., from one busbar to another. The finger under examination is highlighted in blue in Fig. 13 and it corresponds to the finger[2] in blue in Fig. 11(c). The value of the crack opening in correspondence of the considered finger are: 0.13, 0.18, 0.22 and 0.27 μm, for the mid-span deflections of 6, 9, 12 and 15 cm, respectively.

The following parameters of the electric model can be easily identified by matching the experimental values of I_{tt} for a finger not crossed by cracks: $R_{hom} = 0.2\ \Omega\,cm^2$, $V_T = 25$ mV, $\rho_S = 0.13\ \Omega$, $I_{01} = 1.48 \times 10^{-12}$ A/cm^2.

The point of the finger crossed by the crack is at the distance $\xi_{cr} = 6.6$ cm from the lower busbar and it can be identified from the EL images. The value of ξ_0 where the voltage is minimum, and its value V_0, are identified by matching the value of 0.7 V of the voltage at the busbars imposed in the EL test. The localized resistance R_{cr} is identified by matching the jump in the current I_{tt} in correspondence of $\xi = \xi_{cr}$ and in general by minimizing the error between the numerically predicted and the experimental values of I_{tt} along the finger. All the values of the identified parameters are collected in Table 2.

As a general trend, the coordinate ξ_0 of the minimum of the voltage progressively approaches the crack position ξ_{cr} as long as the deformation increases. The localized crack resistance is an increasing function of the crack opening, as shown in Fig. 14. This trend is in agreement with recent experimental results reported in [20], where a glass-based mini-module with a solar cell notched by a laser was subjected to a Mode I three-point bending test. The authors measured the overall back and front size resistances of the solar cell, due to the combined effect of the localized crack and the distributed resistance, along with crack opening measured via a microscope. Although numerical predictions cannot be easily compared with the experimental results, since a single localized resistance is used in the present model instead of two, the same significant increase in the resistance has been noticed in the experiments for crack openings larger than 6 μm. The larger value of crack opening measured in experiments for the minimodule with glass superstrate instead of PET is reasonably due to the presence of residual thermoelastic compressive stresses that in PV modules with glass cover can reach up to 45 MPa [23] and are much higher than in the PET configuration.

5. Conclusions and outlook

A kinematically consistent global/local finite element approach to the simulation of cracking in solar cells embedded in PV modules has been proposed. Via a projection of displacements from the global coarse model of the laminate to the fine-scale local model of the solar cells, it is possible to quantify crack opening of cracks and run fine-scale local analyses in parallel. The computed crack opening displacements obtained by solving the local models can be sequentially transferred as input to the electric model of each finger, for an accurate simulation of the electric response of cracked solar cells.

A parameters identification procedure has been discussed in reference to experimental results obtained by the present authors. The electric resistance vs. crack opening determined by matching the simulated I_{tt} values and the experimental ones is considered to be the first step to determine a robust electromechanical constitutive relation for cracks of the type $R_{cr}(g_n)$, to be applied to all the cracks intersecting fingers. This relation should be independent of boundary conditions and can be used as a constitutive relation for the cracks, as for the cohesive traction-relative displacement relation, or for the heat flux-temperature jump relation.

[2] For interpretation of color in 'Fig. 11', the reader is referred to the web version of this article.

The multi-physics capabilities of the proposed computational approach are essential to understand the physics behind the electric degradation of cracks, which is a phenomenon strongly affected by thermo-mechanical deformation. Nonetheless, the use of a simplified electric model for each finger makes the application of the model feasible and appealing for the photovoltaics community.

In perspective, the proposed model can be used for quality assessment and rejection of cracked PV modules after production. The numerical approach presented here can be in fact used in conjunction with an automatic crack detection algorithm to identify cracks and crack geometries from in-line inspection of EL images. Based on these images, coarse-scale and fine-scale finite element meshes of the PV module can be generated by considering the actual stacking sequence and materials composing the module layers based on manufacturer's specifics. The fine-scale finite element mesh can be generated by an automated meshing software able to deal with an arbitrary number of detected cracks. Global/local simulations finally allow the prediction of the EL signal of each cell in the presence of cracks, based on the proposed electric model and the identified $R_{cr}(g_n)$ relation. The reliability of the numerical predictions can therefore be ascertain with care in comparison with experimental EL images taken in the laboratory. All the model parameters can therefore be tuned in a condition that can be controlled and reproduced. Then, the predictive capabilities of the proposed numerical tool can be explored to simulate the degradation of the electric response of PV module with cracked solar cells under different weathering scenarios that cannot be simulated in the laboratory. This can be done by considering the complex stress state inside the PV module, realistic loading conditions, and the actual orientation of cracks impacting the power-loss in different ways depending on their crack opening and therefore on their orientation with respect to the stress field inside the module.

Acknowledgements

MP would like to acknowledge funding from the European Research Council under the European Union's Seventh Framework Programme (FP/2007-2013)/ERC Grant Agreement No. 306622 (ERC Starting Grant "Multi-field and multi-scale Computational Approach to Design and Durability of PhotoVoltaic Modules" – CA2PVM). The support of the Italian Ministry of Education, University and Research to the Project FIRB 2010 Future in Research "Structural mechanics models for renewable energy applications" (RBFR107AKG) is gratefully acknowledged by MC and IB.

References

[1] Köntges M, Kunze I, Kajari-Schröder S, Breitenmoser X, Bjørneklett B. The risk of power loss in crystalline silicon based photovoltaic modules due to micro-cracks. Solar Energy Mater Solar Cells 2011;95:1131–7.
[2] Kajari-Schröder S, Kunze I, Eitner U, Köntges M. Spatial and orientational distribution of cracks in crystalline photovoltaic modules generated by mechanical load tests. Solar Energy Mater Solar Cells 2011;95:3054–9.
[3] Kajari-Schröder S, Kunze I, Köntges M. Criticality of cracks in PV modules. Energy Proc 2012;27:658–63.
[4] IEA PVPS Task 13. Performance and reliability of photovoltaic systems. Subtask 3.2: review of failures of photovoltaic modules. ISBN: 978-3-906042-16-9.
[5] Duffie JA, Beckman WA. In: Solar engineering thermal processes. Hoboken, NJ: John Wiley & Sons, Inc.; 2013 [chapter 23].
[6] Sander M, Dietrich S, Pander M, Ebert M, Bagdahn J. Systematic investigation of cracks in encapsulated solar cells after mechanical loading. Solar Energy Mater Solar Cells 2013;111:82–9.
[7] Paggi M, Corrado M, Rodriguez MA. A multi-physics and multi-scale numerical approach to microcracking and power-loss in photovoltaic modules. Compos Struct 2013;95:630–8.
[8] Sapora A, Paggi M. A coupled cohesive zone model for transient analysis of thermoelastic interface debonding. Comput Mech 2013;53:845–57.
[9] Pietropaoli E, Riccio A. A global/local finite element approach for predicting interlaminar and intralaminar damage evolution in composite stiffened panels under compressive load. Appl Compos Mater 2011;18:113–25.
[10] Reinoso J, Blàzquez A, Estefani A, París F, Cañas J, Arévalo E, et al. Experimental and three-dimensional global local finite element analysis of a composite component including degradation process at the interfaces. Composites; Part B 2012;43:1929–42.
[11] Reinoso J, Paggi M, Rolfes R. A computational framework for the interplay between delamination and wrinkling in functionally graded thermal barrier coatings. Comput Mater Sci 2015. http://dx.doi.org/10.1016/j.commatsci.2015.08.031. in press.
[12] Eitner U. Thermomechanics of photovoltaic modules (Ph.D. thesis). Zentrum für Ingenieurwissenschaften der Martin-Luther-Universität Halle-Wittenberg; 2011.
[13] Paggi M, Kajari-Schröder S, Eitner U. Thermomechanical deformations in photovoltaic laminates. J Strain Anal Engng Des 2011;46:772–82.
[14] Paggi M, Sapora A. An accurate thermoviscoelastic rheological model for ethylene vinyl acetate based on fractional calculus. Int J Photoenergy 2015 252740.
[15] Paggi M, Reinoso J. An anisotropic large displacement cohesive zone model for fibrillar and crazing interfaces. Int J Solids Struct 2015;69–70:106–20.
[16] Zienkiewicz OC, Taylor RL. The finite element method, 5th ed., vols. 1–3. Oxford, UK: Butterworth-Heinemann; 2000.
[17] Breitenstein O, Rißland S. A two diode model regarding the distributed series resistance. Solar Energy Mater Solar Cell 2013;110. 77–6.
[18] Berardone I, Corrado M, Paggi M. A generalized electric model for mono and polycrystalline silicon in the presence of cracks and random defects. Energy Proc 2014;55:22–9.
[19] Paggi M, Berardone I, Infuso A, Corrado M. Fatigue degradation and electric recovery in Silicon solar cells embedded in photovoltaic modules. Sci Rep 2014;4:4506. http://dx.doi.org/10.1038/srep04506.
[20] Käsewieter J, Haase F, Larrodé MH, Köntges M. Cracks in solar cell metallization leading to module power loss under mechanical loads. Energy Proc 2014;55:469–77.
[21] Fuyuki T, Kondo H, Kaji Y, Ogane A, Takahashi Y. Analytic findings in the electroluminescence characterization of crystalline silicon solar cells. J Appl Phys 2007;101:023711.
[22] Tvergaard V. Effect of fiber debonding in a whisker-reinforced metal. Mater Sci Engng A 1990;107:23–40.
[23] Ojo SO, Paggi M. A thermo-visco-elastic shear-lag model for the prediction of residual stresses in photovoltaic modules after lamination. Compos Struct 2016;136:481–92.